Supplementary material for the article:

Chen, J.; Stepanovic, S.; Draksharapu, A.; Gruden, M.; Browne, W. R. A Non-Heme Iron Photocatalyst for Light-Driven Aerobic Oxidation of Methanol. *Angewandte Chemie - International Edition* **2018**, *57* (12), 3207–3211. https://doi.org/10.1002/anie.201712678

Angewandte Chemie
Eine Zeitschrift der Gesellschaft Deutscher Chemiker

Supporting Information

A Non-Heme Iron Photocatalyst for Light-Driven Aerobic Oxidation of Methanol

Juan Chen, Stepan Stepanovic, Apparao Draksharapu, Maja Gruden,* and Wesley R. Browne**

anie_201712678_sm_miscellaneous_information.pdf

Contents

Experimental Section

1,1-di(pyridin-2-yl)-N,N-bis(pyridin-2-ylmethyl)ethan-1-amine (MeN4Py),[1] $[(N4Py)Fe^{II}(CH_3CN)](ClO_4)_2$ (**1**),[2] and $[(MeN4Py)Fe^{III}(OCH_3)](ClO_4)_2$ (**2**),[1] were prepared by previously reported procedures. Commercially available chemicals were purchased from Sigma Aldrich without further purification. All solvents used for spectroscopy were of UVASOL (Merck) grade. $[(MeN4Py)Fe^{III}(Cl)](ClO_4)_2$ (**3**) was prepared by mixing equimolar amounts of $Fe^{III}Cl_3$ and the ligand (MeN4py) in acetonitrile, followed by addition of 10 equiv. $NaClO_4$ in a minimum amount of acetonitrile. Vapour diffusion of diethyl ether into the solution at room temperature provided signal crystals of $[(MeN4Py)Fe^{III}(Cl)](ClO_4)_2$. Complex $[(MeN4Py)Fe^{III}\text{-}O\text{-}Fe^{III}(MeN4Py)](ClO_4)_4$ (**2a**) were obtained by slow evaporation of a concentrated solution of $[(MeN4Py)Fe^{III}(Cl)](Cl)_2$[3] in water with added $LiClO_4$.

A single crystal of compound **3** was mounted on top of a cryoloop and transferred into the cold nitrogen stream (100 K) of a Bruker-AXS D8 Venture diffractometer. Data collection and reduction was done using the Bruker software suite APEX3.[4] The final unit cell was obtained from the xyz centroids of 9752 reflections after integration. A multiscan absorption correction was applied, based on the intensities of symmetry-related reflections measured at different angular settings (SADABS). The structures were solved by direct methods using SHELXS, and refinement of the structure was performed using SHLELXL. The hydrogen atoms were generated by geometrical considerations, constrained to idealised geometries and allowed to ride on their carrier atoms with an isotropic displacement parameter related to the equivalent displacement parameter of their carrier atoms. The structure was refined as a two-component inversion twin. Crystal data and details on data collection and refinement are presented in Table S1

Physical methods UV-vis absorption spectra were recorded with a Specord 600 (AnalytiJena) spectrometer in 1 cm path length quartz cuvette. ESI mass spectra of complexes were recorded on a Triple Quadrupole LC/MS/MS mass spectrometer (API 3000, PerkinElmer Sciex Instruments). Electrochemical measurements were carried out by a model CHI760B Electrochemical workstation (CH Instruments) in acetonitrile with 0.1 M $TBAPF_6$, a 3 mm diameter Telflon-shrouded glassy carbon, a Pt wire, and an SCE electrode, were used as working, counter and reference electrode, respectively. EPR (X-band, 9.46 GHz) were recorded on a Bruker ECS106 spectrometer in liquid nitrogen (77K). Samples (0.4 mL), monitored by UV-vis absorption spectroscopy, were flash frozen in liquid nitrogen. FTIR spectra were recorded using a UATR (ZnSe) with a Perkin Elmer Spectrum400, equipped with a liquid nitrogen cooled MCT detector. Raman spectra were recorded at λ_{exc} 785 nm using a Perkin Elmer Raman Station at room temperature. Raman spectra at 355 nm (10 mW at source, Cobolt Lasers) were acquired in a 180° backscattering arrangement. Raman scattering was collected by a 2.5 cm diameter plano convex lens (f = 7.5 cm). The collimated Raman scattering passed through an appropriate long pass edge filter (Semrock) and was focused by a second 2.5 cm diameter plano convex lens (f = 15 cm) into a Shamrock500i spectrograph (Andor Technology) 2400 L/mm grating blazed at 300 nm, respectively, acquired with an iDus-420-BU2 CCD camera (Andor Technology). The spectral slit width was set to 12 µm. Data were recorded and processed using Solis (Andor Technology) and Spectragryph with spectral calibration performed using the Raman spectrum of acetonitrile/toluene, 50:50 (v/v).

Irradiation Typically 2 mL of **1-3** (0.125 mM) in solvent were purged with Ar in a 1 cm pathlength cuvette for 5 min before irradiation to remove oxygen. Irradiation was carried out orthogonally to the monitoring beam of the UV-vis absorption spectrometer. LEDs (Thorlabs) were used at 365 nm (M365 F1, 6.10×10^{-5} einstein s^{-1} dm^{-3}), 490 nm (M490F3, 4.76×10^{-6} einstein s^{-1} dm^{-3}), 565 nm (M565F, 3.19×10^{-6} einstein s^{-1} dm^{-3}), and 300 nm (M300F2, 1.25 ×

10^{-6} einstein s^{-1} dm^{-3}) controlled by T-Cube Light Source & Driver Module (Thorlabs); or a DPSS laser at 355 nm (9.79 × 10^{-6} einstein s^{-1} dm^{-3}, Cobolt Lasers). Light intensity at sample was measured with PM10V1 High Power 10 Watt sensor coupled to a FieldMate Power Meter. Quantum yields were calculated according to literature methods with modification for the photo-reduction process.[5,6]

Quantification of formaldehyde formation. Formaldehyde was quantified[7] colourimetrically. 0.5 mL of reaction solution was diluted with H_2O by between 10 to 20 times (depending on the expected final absorbance) and 1 mL of the diluted solution was mixed with 1 mL of the reagent solution {NH_4OAc (15 g, 0.19 mol), acetic acid (0.3 mL, 5.4 mol) and pentane-2,4-dione (0.2 mL, 1.9 mol) in 100 mL water}. Standard solutions were prepared with known concentrations (0.125, 0.25, 0.5, 1.0, and 2 mM) containing formaldehyde and 0.5 mL of these solutions mixed with 0.5 mL of H_2O and 1 mL reagent solution. Samples were held at 31 °C in a temperature controlled cuvette holder and monitored by UV-vis absorption spectroscopy, until the absorbance at 412 nm did not increase further. The concentration of formaldehyde in the reaction mixtures was calculated from the calibration curve obtained.

Computational details All DFT calculations were performed with the Amsterdam Density Functional (ADF) suite of program (unless otherwise indicated).[8,9] MOs were expanded in an uncontracted set of Slater type orbitals (STOs) of triple-zeta quality containing diffuse functions and two sets of polarization functions(TZ2P).[10] Full electron basis sets were used in all calculations. An auxiliary set of s, p, d, f, and g STOs were used to fit the molecular density and to represent the Coulomb and exchange potentials accurately for each SCF cycle. Geometries were optimized until the maximum gradient component was less than 5·10-4 a.u. (default value is 10-3 a.u.). Energies and gradients were calculated using the several density functional approximations (DFAs) based on generalized gradient approximation, GGA (BP86,[11,12] OPBE,[13,14] PBE,[15,16] PW91[15,17–19] and S12g[20]), hybrid DFAs (B3LYP,[21] PBE0[22] and S12h[20]), meta-GGA DFAs(M06-L[23,24] and TPPS[25]) and metahybrid DFAs (M06[24] and M06-2X[24]). Since S12g DFA gave by far the best structural data, all further electronic structure calculations were performed with this level of theory, with Becke grid[26,27] numerical accuracy of verygood quality. COSMO[28–30] dielectric continuum model was used for implicit treatment of the environment (with acetonitrile as a solvent).[31,32] Scalar relativistic corrections have been included self-consistently by using the zeroth-order regular approximation (ZORA).[33–35] The nature of the stationary points is confirmed by calculating analytical Hessians, with S12g/COSMO level of theory.

Additional Figures and Tables

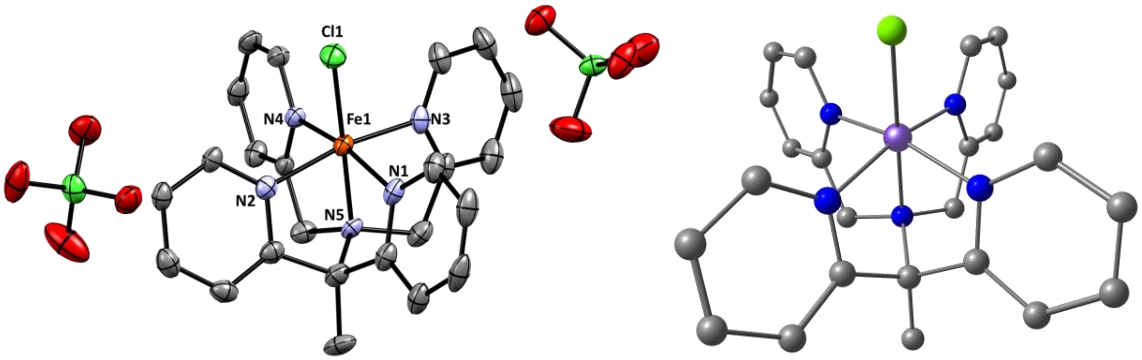

Figure S 1. (Left) ORTEP plots of structure of complex [(MeN4Py)Fe^{III}Cl](ClO$_4$)$_2$ (**3**), showing 50% probability ellipsoids. Hydrogen atoms are omitted for clarity. Crystal data and a list of selected bond lengths and angles are reported in Tables S1. Hydrogen atoms are omitted for clarity. (right) DFT optimized (S12g/TZ2P) structure of **3**.

Table S 1**.** Crystallographic data for **3**

chem formula	C24 H23 Cl3 Fe N5 O8
M_r	671.67
cryst syst	orthorhombic
color, habit	orange, platelet
size (mm)	0.29 x 0.28 x 0.06
space group	$Pna2_1$
a (Å)	14.9402(8)
b (Å)	10.6123(5)
c (Å)	16.3170(9)
V (Å^3)	2587.1(2)
Z	4
ρ_{calc}, g.cm^{-3}	1.724
μ(Mo K$\bar{\alpha}$), cm^{-1}	0.954
F(000)	1372
temp (K)	100(2)
θ range (deg)	2.999 – 28.371
data collected (h,k,l)	-19:19, -14:14, -21:21
no. of rflns collected	47935
no. of indpndt reflns	6432
observed reflns	5572 ($F_o \geq 2\,\sigma(F_o)$)
R(F) (%)	4.08

wR(F^2) (%)	9.71
GooF	1.037
Weighting a,b	0.0462, 2.4261
params refined	372
restraints	1
min, max resid dens	-0.368, 0.642

Table S 2 Comparison of bond lengths (Å) in the optimized structures (S12g/TZ2P) of **3** with those obtained by single crystal X-ray analysis.

		DFT calculation	experimental
Bond length	Fe1-Cl1	2.191	2.211
	Fe1-N1	1.970	1.961
	Fe1-N2	1.970	1.973
	Fe1-N3	1.987	1.969
	Fe1-N4	1.987	1.968
	Fe1-N5	1.999	1.964
Bond angle	C1-Fe1-N5	176.74	175.46

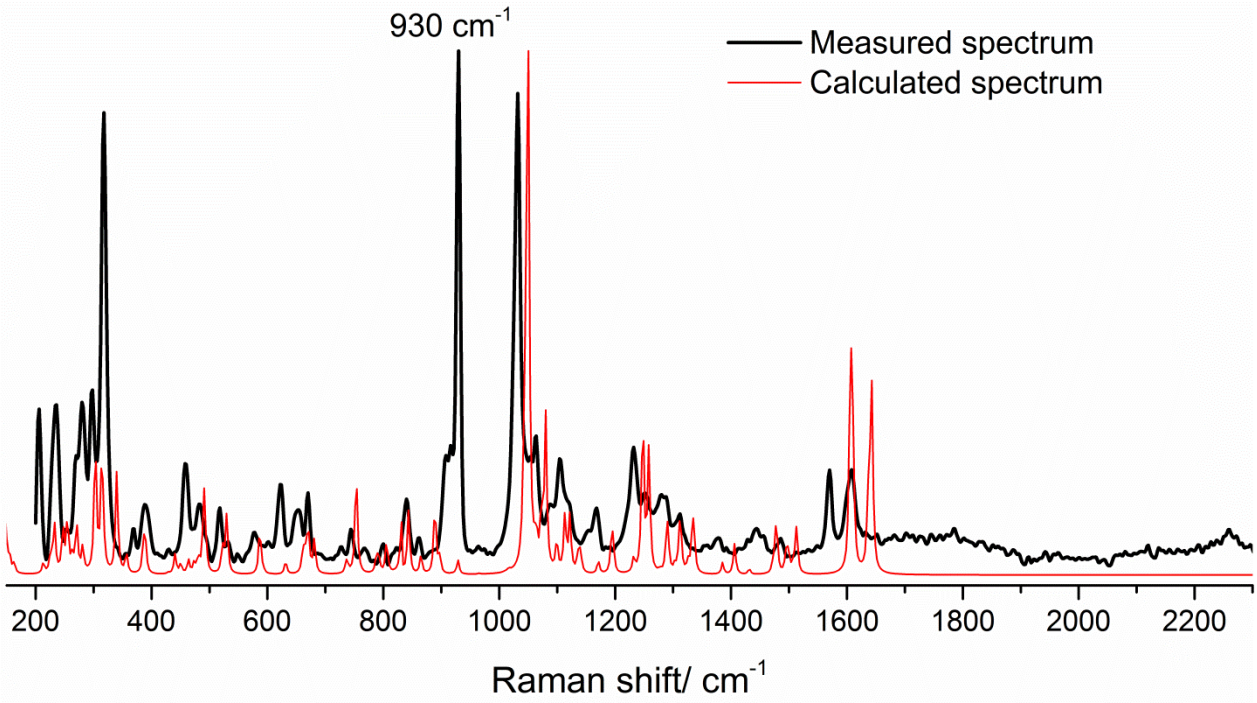

Figure S 2. Comparison of experimental Raman spectrum (λ_{exc} 785 nm) of **3** in the solid state with the calculated spectrum (by Gaussian 09, Revision D.01, using an unrestricted hybrid density functional UB3LYP5 combined with CEP-31G6 basis set for iron and 6-311+g(d,p) for the rest of the atoms); 930 cm^{-1} is a Cl=O stretching from ClO_4^- counter iron.[36]

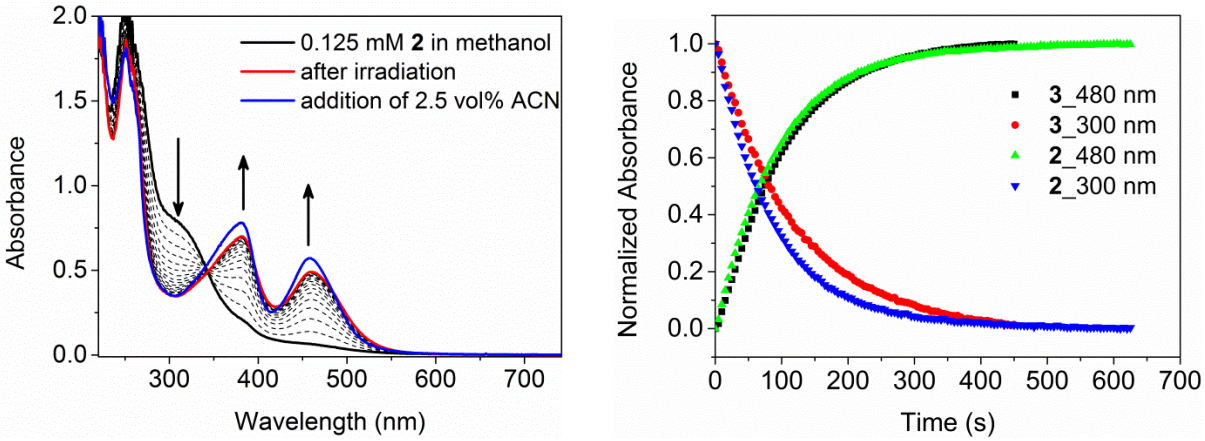

Figure S 3. Left. UV-vis absorption spectrum of **2** (0.125 mM, black solid line) in argon purged methanol, during (dotted lines) and after (red solid line) irradiation at 365 nm, and after subsequent addition of 2.5 vol % acetonitrile (black dashed line). Absorbance changes at 300 and 480 nm of **2** and **3** (0.125 mM) (right) in deoxygenated methanol over time under irradiation (λ_{exc} 365 nm). The absorbance at 300 nm is normalised at t = 0 s and at 480 nm at t = 600 s.

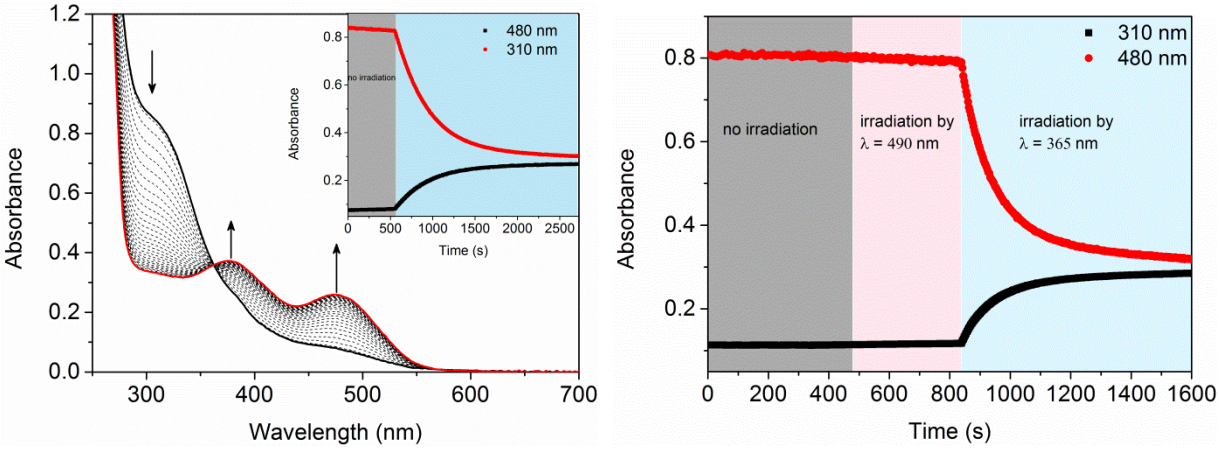

Figure S 4. (left) UV-vis absorption spectrum of **3** in deoxygenated methanol (black line) under irradiation at 300 nm (inset shows the absorbance at 310 and 480 nm with time). Right: Absorbance at 310 and 480 nm over time with initially no irradiation, irradiation at 490 nm and at 365 nm.

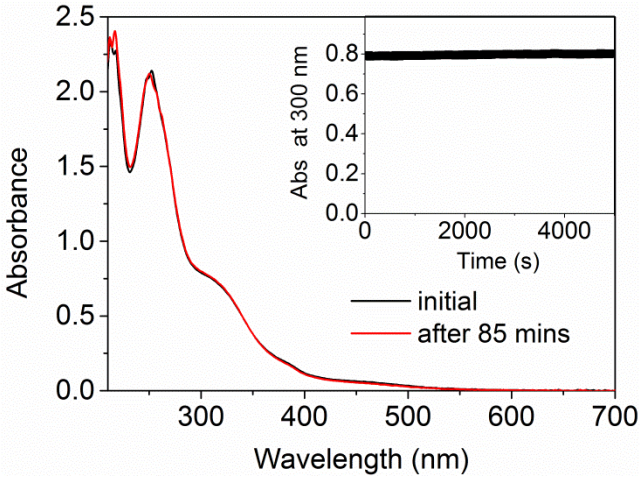

Figure S 5. UV-vis absorption spectrum of **2** (0.125 mM) in deoxygenated methanol at 0 and 85 min without irradiation. Inset shows the absorbance at 300 nm over time.

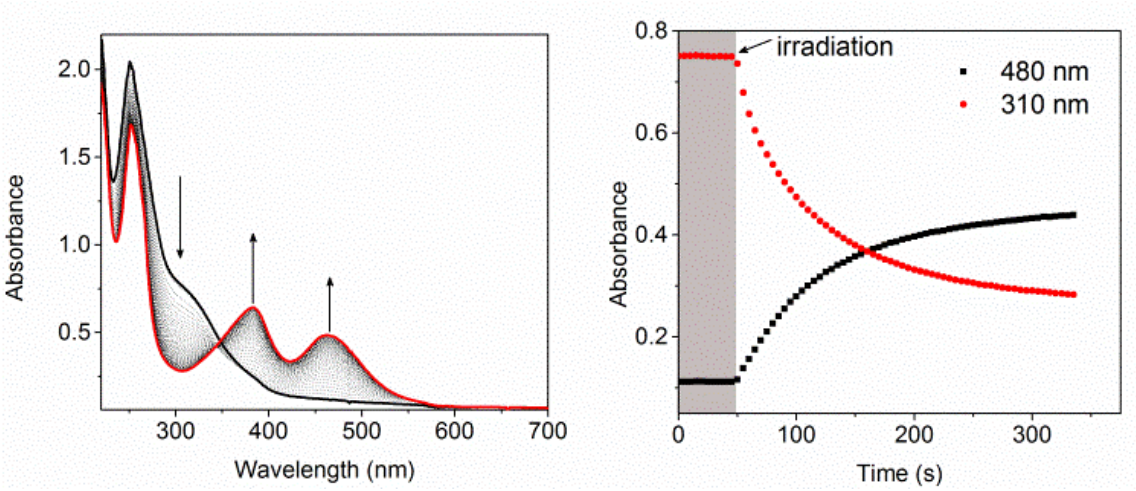

Figure S 6. Left: UV-vis absorption spectrum of **2a** (0.0625 mM) in deoxygenated methanol under irradiation at 365 nm. Right: Absorbance at 310 and 480 nm over time in the dark and under irradiation.

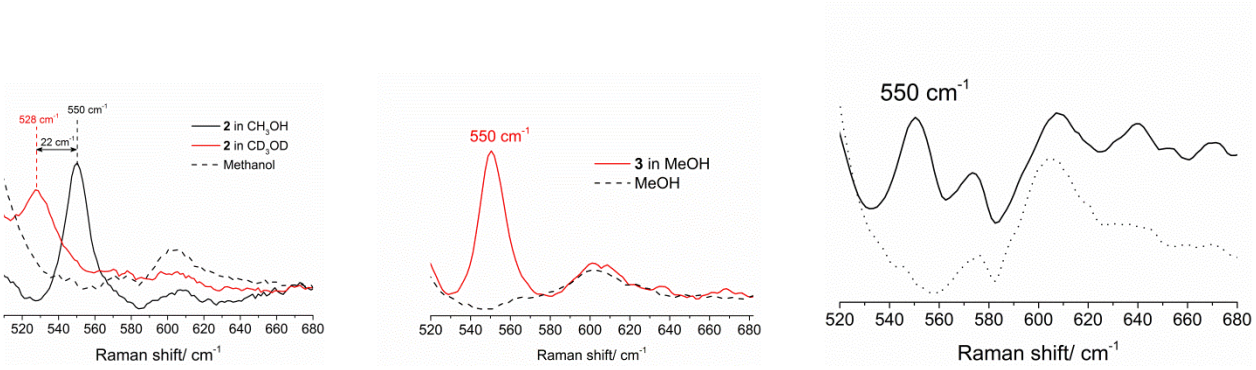

Figure S 7. Resonance Raman (λ_{exc} 355 nm) spectrum of **2** (left), **3** (middle) and **2a** (right) in methanol; the band at 550 cm^{-1} was assigned to Fe-O stretching mode in $[(MeN4Py)Fe\text{-}OMe]^{2+}$ by comparison of the spectrum in CH_3OH and CD_3OD (with CH_3OD there is no isotopically induced shift of the 550 cm^{-1} band).

Comments on the solution chemistry of complexes 2 and 3

The similar photoreactivity observed for **2** and **3** (and **1**) is unsurprising considering that they all show essentially identical UV-vis absorption spectra in methanol, as well as S = ½ EPR signals (X-band, at 77 K) at g = 2.29, 2.12, 1.98 (**Figure S 8**), which is characteristic of the low spin complex $[(MeN4Py)Fe^{III}\text{-}OMe]^{2+}$,The ESI mass spectrum of **3** in methanol has a base signal at m/z 234.3 and a weaker signal at m/z 567.3, corresponding $[(MeN4Py)Fe^{III}\text{-}OCH_3]^{2+}$ and $\{[(MeN4Py)Fe^{III}\text{-}OCH_3](ClO_4)\}^{+}$, respectively. Resonance Raman (λ_{exc} 355 nm) spectra (**Figure S 7**), shows bands at 550 cm^{-1}, assigned to Fe-(OCH_3) stretching mode of $[(L)Fe\text{-}OCH_3]^{2+}$, confirmed isotope ($OD_3$) shift (**Figure S 7)**. Hence the data confirm that methanol displaces the Cl^- ligand upon dissolving **3** in methanol.

The Fe^{II} complex obtained upon irradiation of **3** has a lower visible absorbance than for **2,** due to preference for Cl^- binding over MeO^- in the Fe^{II} state, verified by addition of 2 equiv. NaCl to **1** in methanol (**Figure S 10**).

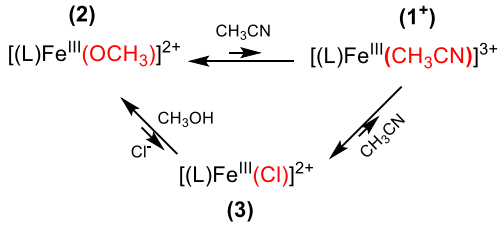

Scheme S 1**.** Ligand exchange reactions of complexes **2,** and **3** in methanol and acetonitrile. In the Fe^{III} oxidation state the coordination of CH_3CN is unfavourable.-.

In acetonitrile **3** is EPR (X band) silent even at 4 K (**Figure S 11Error! Reference source not found.**) and has a paramagnetically broadened and shifted ^{1}H-NMR spectrum (**Figure S 12**). The Fe-O stretching band that is observed in the spectra of **2** (Figure S 7) is absent in the Raman (λ_{exc} 355 nm) spectrum of **3** and the absorption band at 320 nm is more intense than observed for **2**. These data indicate that the chloride ligand of **3** remains bound. In acetonitrile, **3** undergoes an electrochemically reversible (but partially chemically irreversible due chlorido/acetonitrile exchange in the ferrous state) oxidation at 0.49 V vs SCE characteristic of the $[(L)Fe^{III}/Fe^{II}\text{-}Cl]$ couple (**Figure S 13**),[37] which is less positive than that of the $[(L)Fe^{III}/Fe^{II}\text{-}CH_3CN]$ couple (1.1 V vs SCE).[1] The ligand exchange reactions are summarized in Scheme S 1.

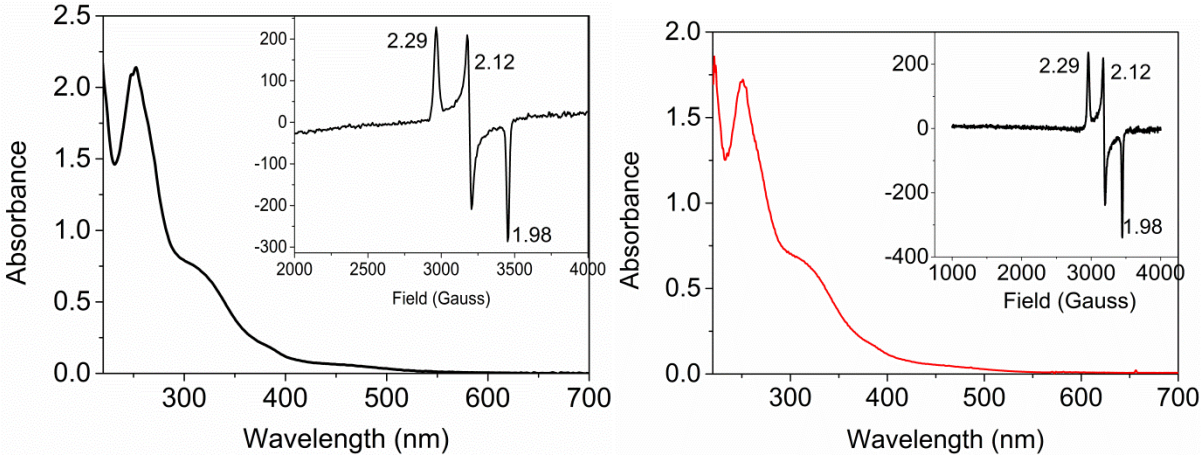

Figure S 8. UV-vis absorption spectra of **2** (left) and **3** (right) in methanol; X-band EPR spectra at 77 K are shown as insets.

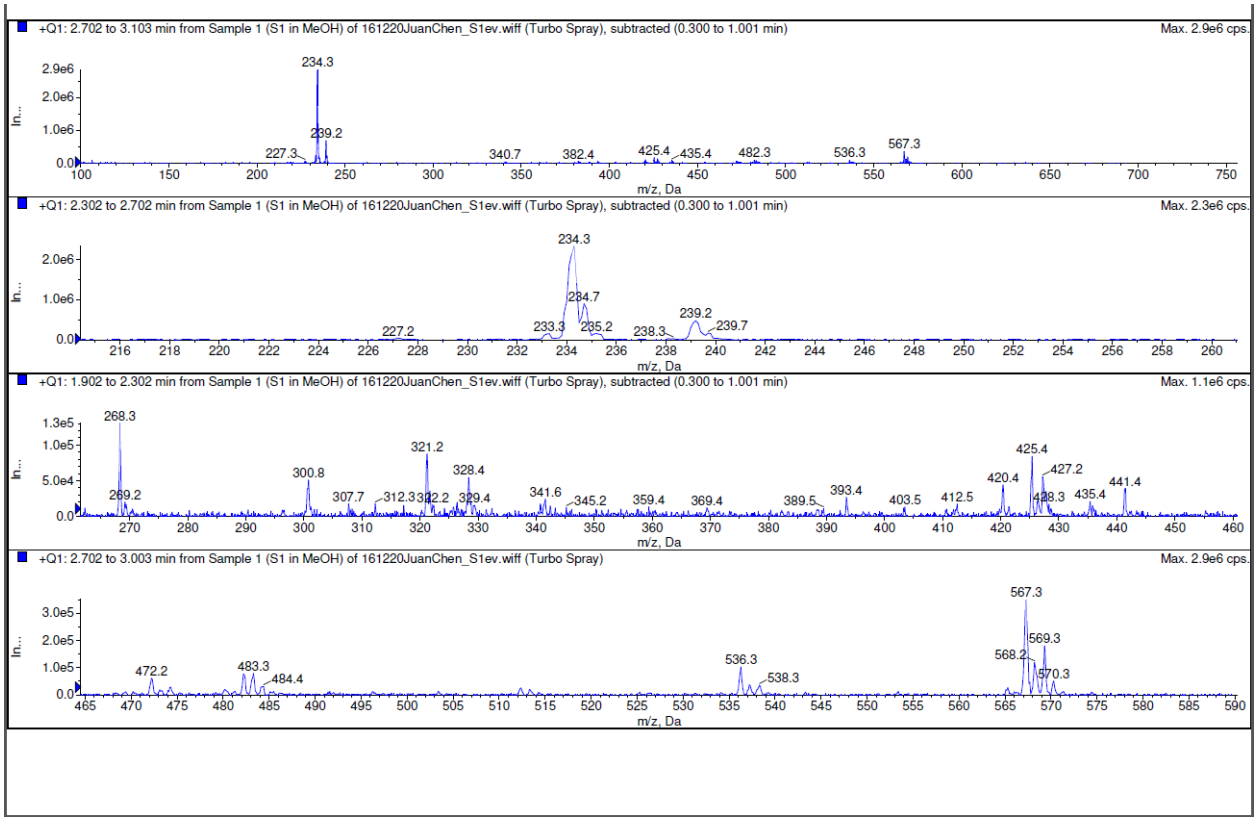

Figure S 9. ESI mass spectra of **3** in methanol.

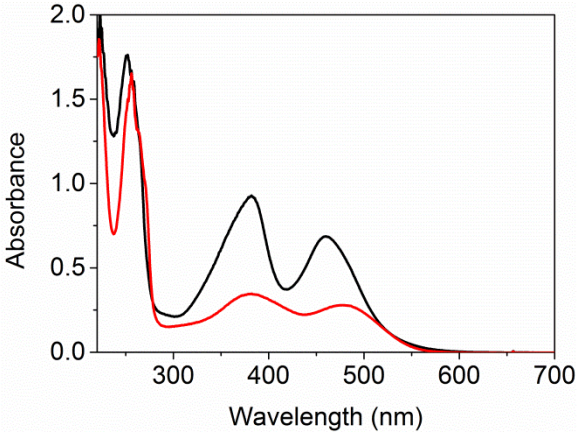

Figure S 10. UV-vis absorption spectrum of **1** (0.125 mM) in methanol before (black) and after (red) addition of 2 equiv. NaCl.

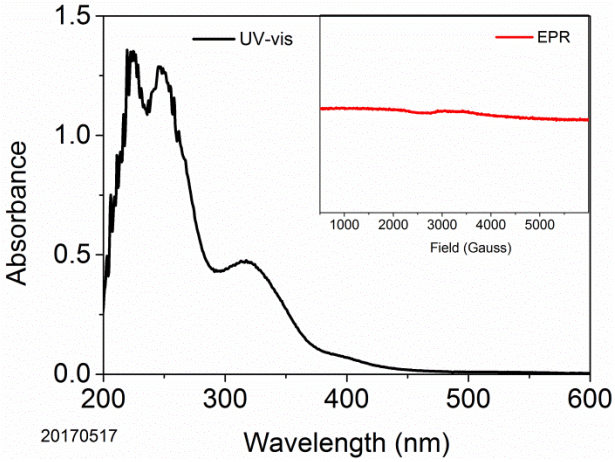

Figure S 11 UV-vis absorption spectrum of **3** in acetonitrile, X-band EPR spectrum at 77 K is shown as an inset.

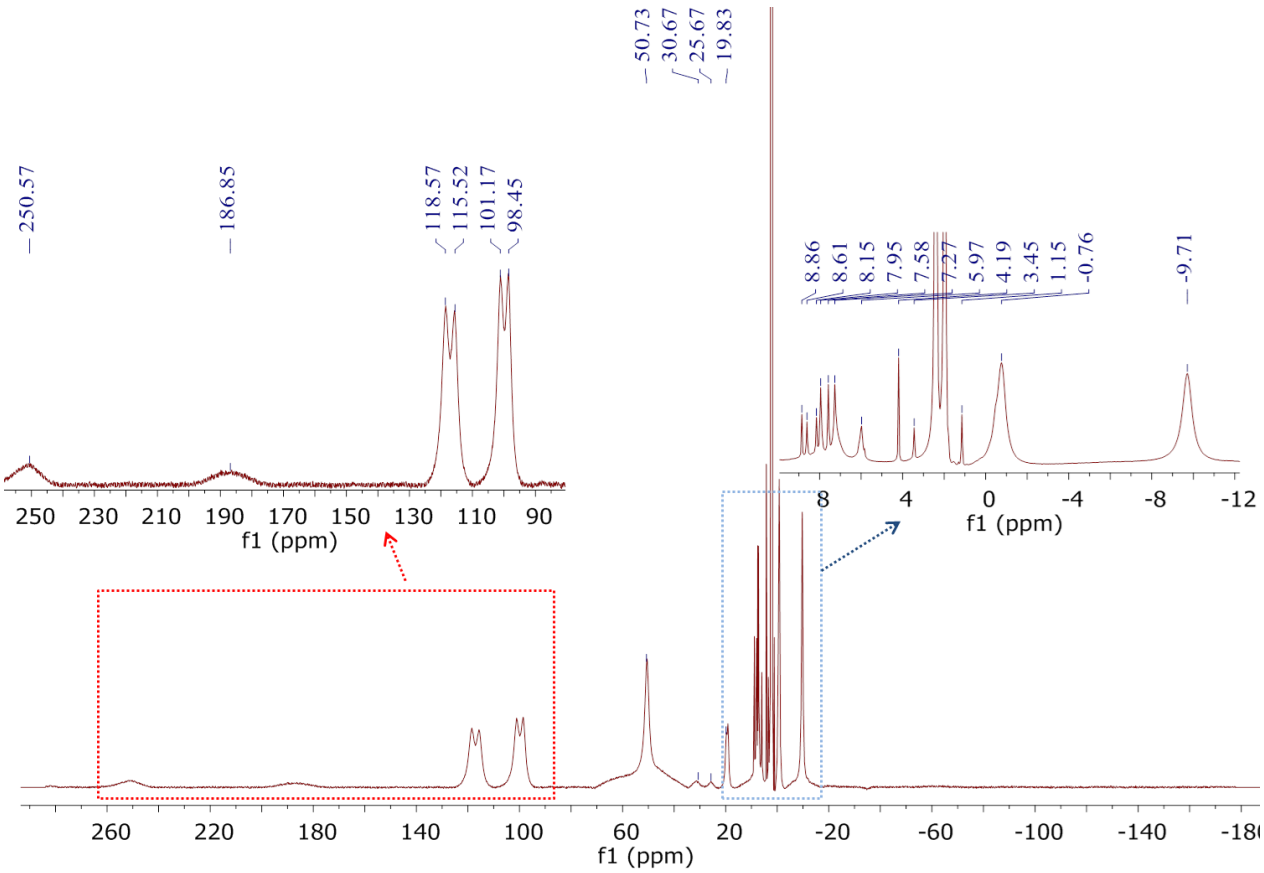

Figure S 12. ^{1}H NMR spectrum of **3** in CD_3CN.

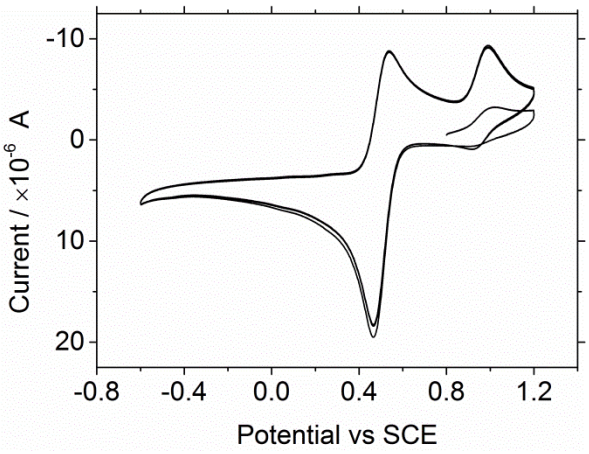

Figure S 13. Cyclic voltammetry of **3** (**1** mM) in acetonitrile (0.1 M $TBAPF_6$), scan rate 0.1 V s^{-1}.

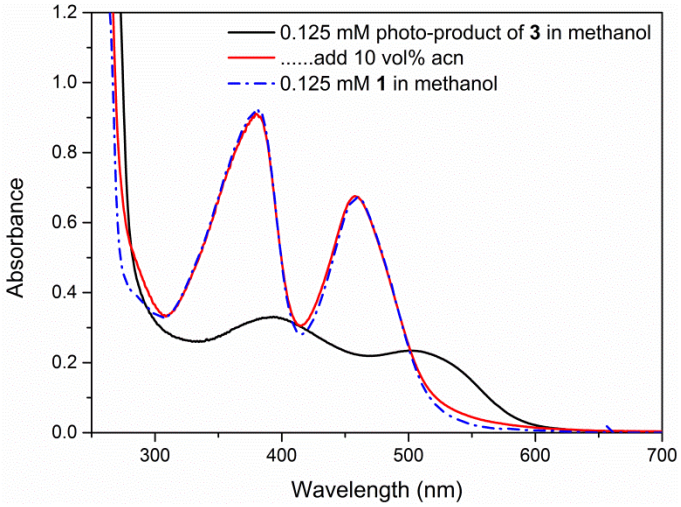

Figure S 14. UV-vis absorption spectrum of the photo-product obtained upon irradiation of **3** in argon purged methanol at 365 nm (black solid line), after addition of 10 vol% of acetonitrile (red solid line); 0.125 mM $[(Men4py)Fe^{II}(CH_3CN)]^{2+}$ (**1**) in acetonitrile.

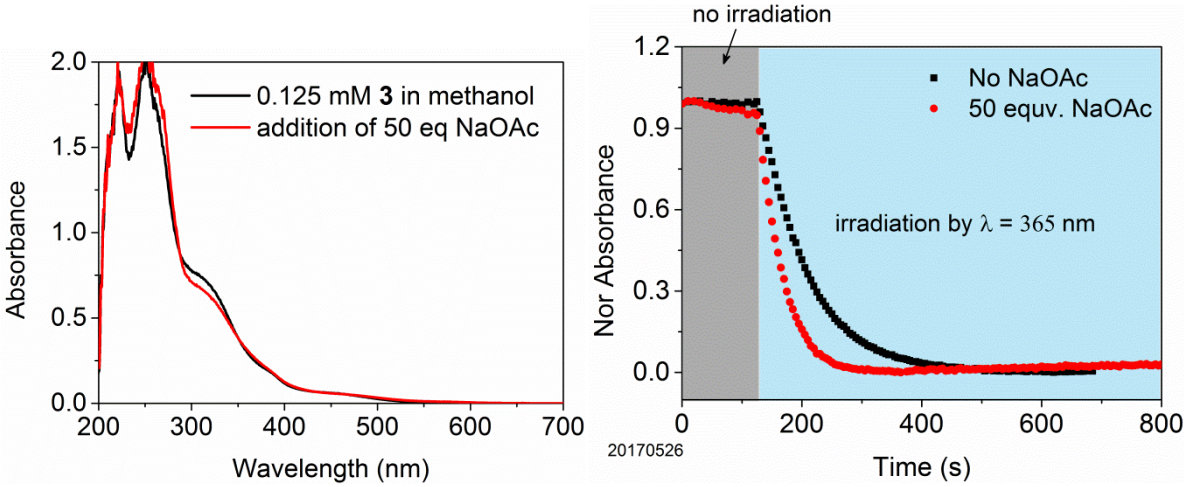

Figure S 15 (Left) UV-vis absorption spectrum of **3** (0.125 mM) in methanol with (red) and without (black) NaOAc (6.25 mM). (Right) Normalized absorbance at 310 nm over time in the dark and under irradiation at 365 nm with (red) and without (black) NaOAc (6.25 mM).

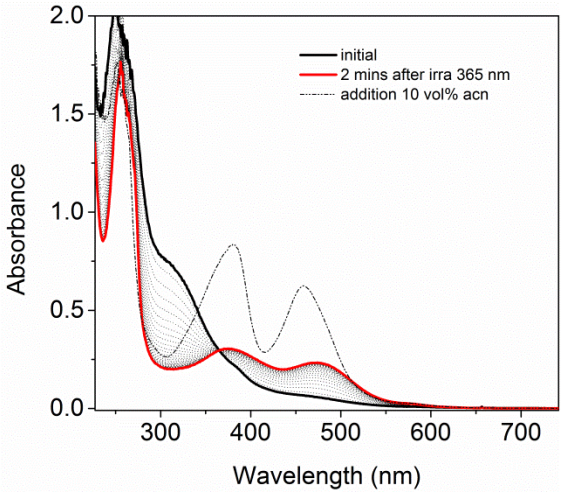

Figure S 16. UV-vis absorption spectrum of **2** (0.125 mM) in deoxygenated methanol with NaOAc (6.25 mM), before (black solid line), during (dashed lines) and after (red line) irradiation at 365 nm and after addition of 10 vol % of acetonitrile (dashed black line).

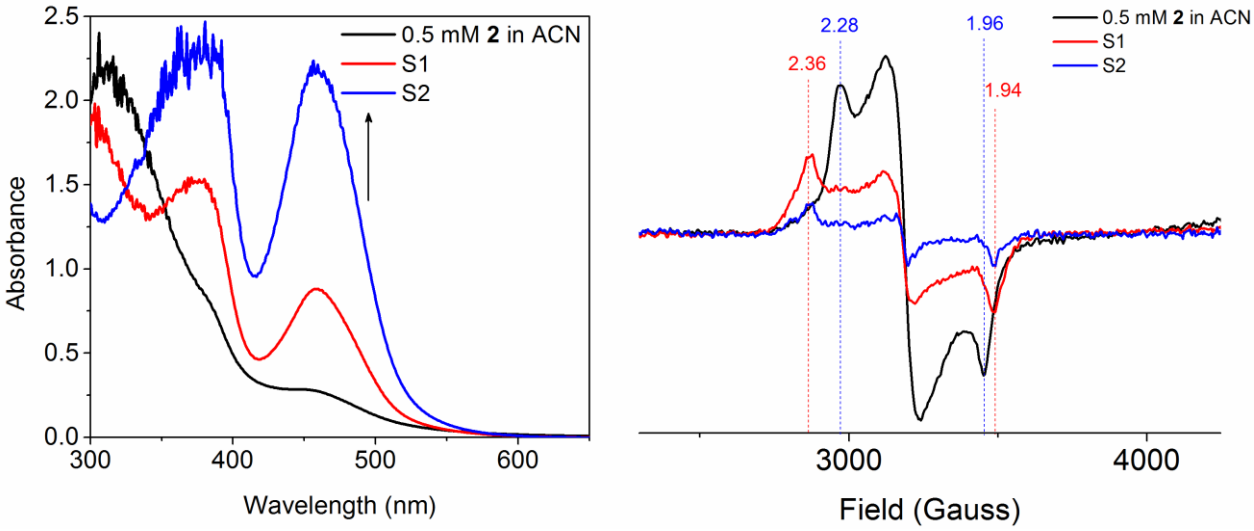

Figure S 17. (left) UV-vis absorption spectrum of **2** (0.5 mM) in acetonitrile before (black) and during (red) and after (blue) irradiation at 365 nm. (right) X-band EPR spectra of corresponding samples rapidly frozen in liquid nitrogen (77 K). g = 2.28, 2.12, 1.96 are the characteristic signals of $[(MeN4Py)Fe^{III}(OCH_3)]^{2+}$ (**2**) and at g = 2.36, 2.16, 1.94 of $[(MeN4Py)Fe^{III}\text{-}OH]^{2+}$.

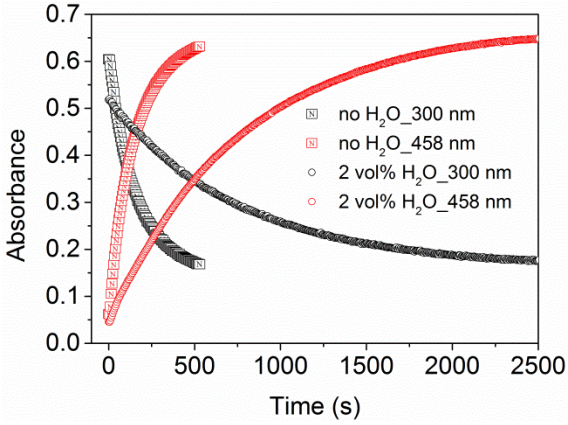

Figure S 18. Absorbance at 300 and 458 nm of **2** in deoxygenated acetonitrile under irradiation (λ_{exc} 365 nm) in the absence and presence of 2% H_2O (v/v).

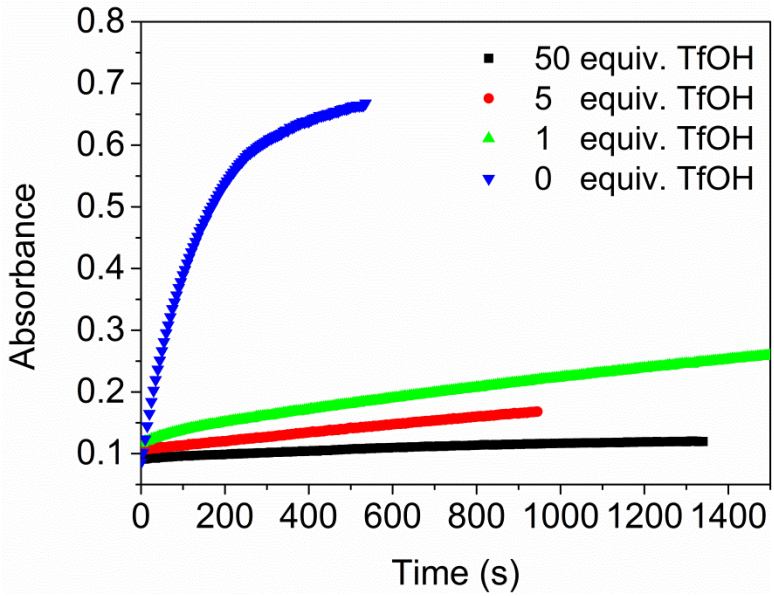

Figure S 19. Absorbance at 458 nm of **2** (0.125 mM) in deoxygenated acetonitrile over time under irradiation at 365 nm with 0 (blue), 1 (green), 5 (red) and 50 (black) equiv. triflic acid.

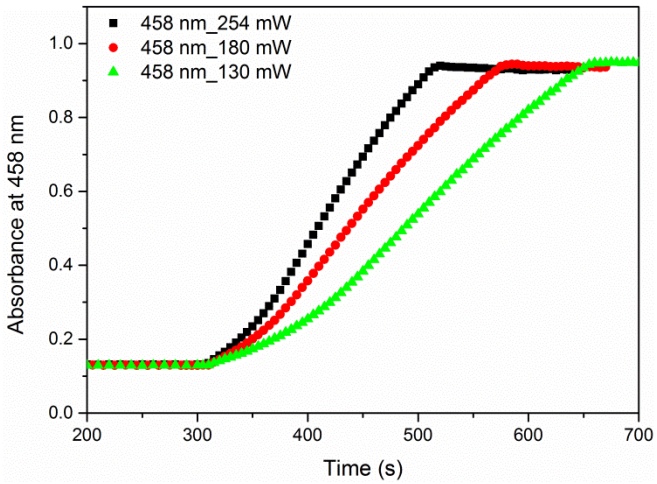

Figure S 20. Absorbance at 458 nm over time under irradiation (from 300 s) of **3** in deoxygenated acetonitrile at 365 nm (130 mW – 254 mW).

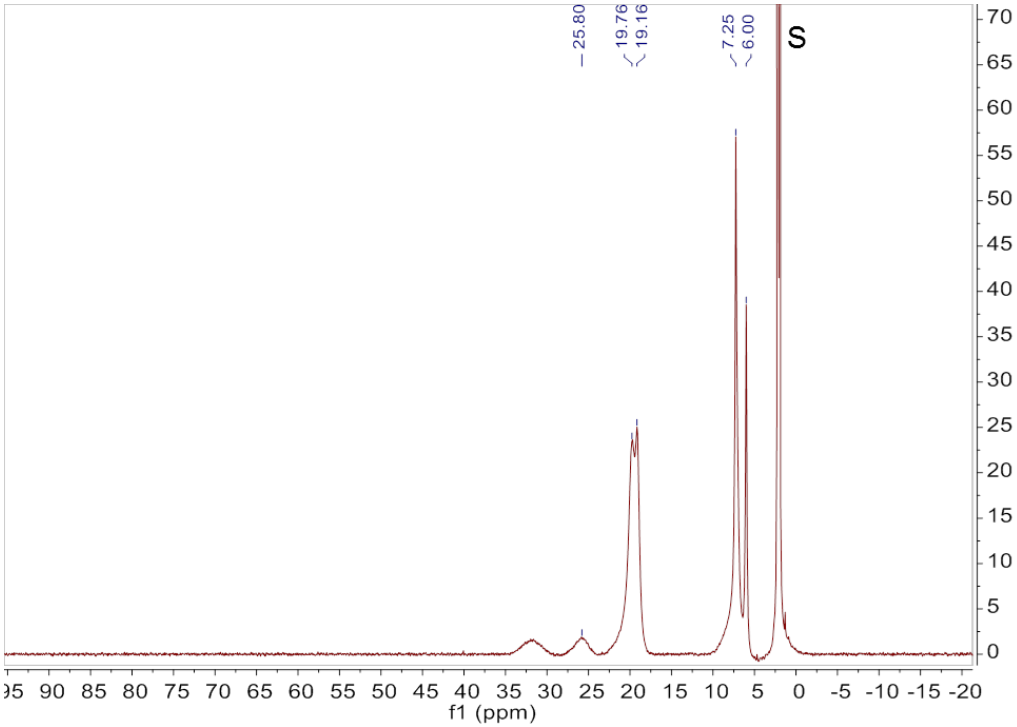

Figure S 21. ^{1}H-NMR spectrum of [(MeN4Py)Fe^{III}-μ-O-Fe^{III}(MeN4Py)]$^{4+}$ (**2a**) in CD_3CN, solvent (S) was labelled.

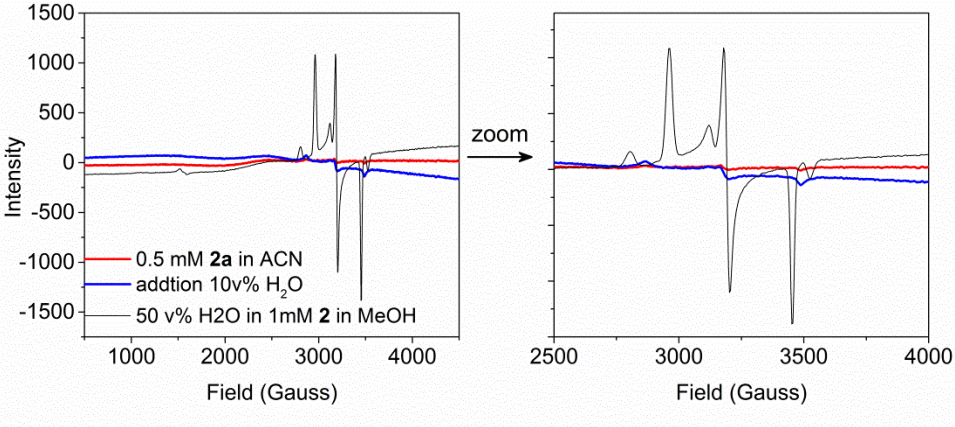

Figure S 22. (left) X-band EPR spectra of **2a** (0.5 mM) in anhydrous acetonitrile (red) in liquid nitrogen (77 K); addition of 10 vol% H_2O (blue), and EPR of the 1 mM monomer iron(III).

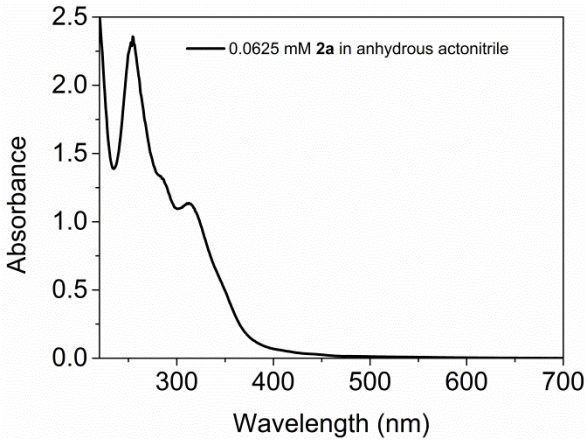

Figure S 23.. UV-vis spectra of **2a** (0.0625 mM) in anhydrous acetonitrile

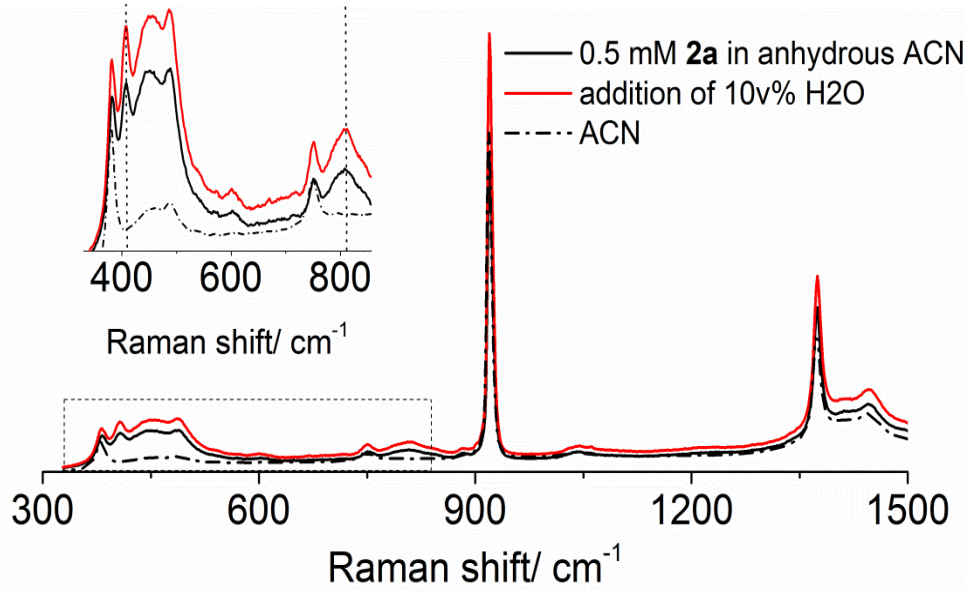

Figure S 24. Resonance Raman (λ_{exc} 355 nm) spectrum of **2a** (0.5 mM) in acetonitrile, before and after addition of 10 vol% H_2O.

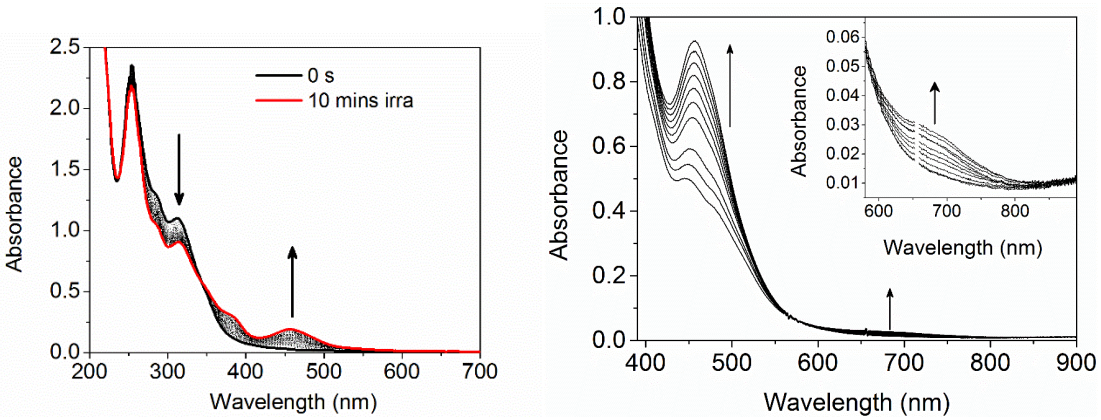

Figure S 25. UV-vis spectrum changes under irradiation (365 nm) of **2a** (left: 0.0625 mM, right: 0.5 mM) in anhydrous acetonitrile.

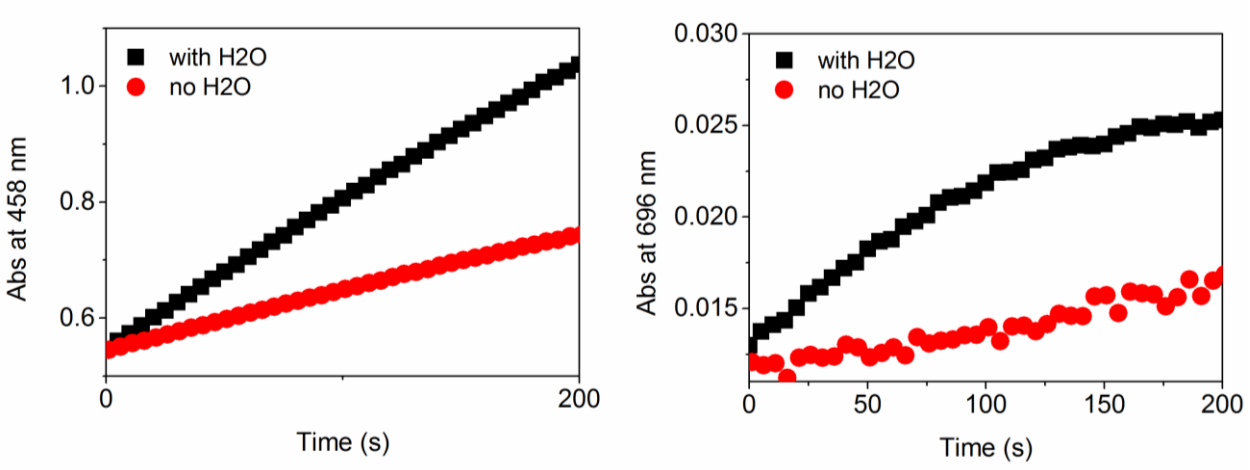

Figure S 26. Comparison of the corresponding absorbance changes at 458 and 686 nm of **2a** in acetonitrile under irradiation with and without present of 10V% H_2O

Discussion of Computational studies and details of methods and data

The performance of 12 density functional approximations (DFAs, Table S3) indicated that S12g[20] was most appropriate to describe structural parameters in the present systems. Inspection of the electronic structure of the μ-oxido bridged dinuclear complex **2a** and all accessible spin states, revealed an antiferromagnetically coupled ground state (Table S4), in accordance with the experimental data.[2]

Inspection the ground state of Fe^{III}-μ-O-Fe^{III} (Scheme S2), indicates that MOs originating from d-orbitals can be deduced by combining two separate Fe(III) spin centers. It follows that all occupied MOs in α-spin are located on one Fe(III) center while the virtual orbitals are predominantly on the other, as a consequence of the localized nature of the BS description (Scheme S2).

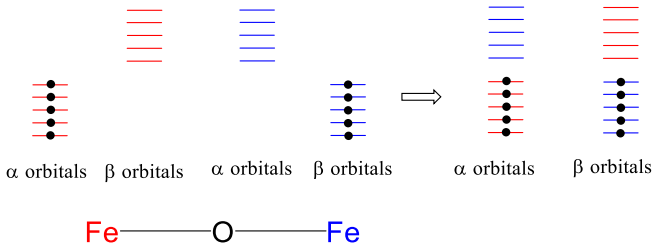

Scheme S2. Description of two monomeric iron centres in the framework of the BS approximation as separate units (left) and as a pair showing a localized description of MO of [(L)Fe^{III}-μ-O-Fe^{III}(L)]$^{2+}$(**2a**).

The consequence of photoexcitation of the Fe^{III}-μ-O-Fe^{III} complex was examined on the basis of single excitation from the S = 0 ground state of the separated centres followed by coupling the centres to obtain the total spin. Note that the two Fe^{III} centers are in their maximum multiplicity, and there is only one sextet state in the d^5 manifold ($^6A_{1g}$ in O_h symmetry), hence spin allowed transitions are not available within one center excitations. The spin forbidden transition produces a spin 3/2 (IS) state on one of the iron centre, and the total spin is: S(5/2,3/2) = 5,4,3,2,1. Charge transfer generates a Fe^{II}(HS)-Fe^{IV}(HS) coupled dimer, i.e. two S = 2 centres, and the resulting total spin is: S(2,2) = 4,3,2,1,0. Hence we can conclude that a spin allowed d-d excitation from the S = 0 ground state of two coupled HS Fe^{III} centres can only lead to charge transfer generating a Fe^{II}-Fe^{IV} dimer. Additionally, the spin forbidden transition can form either Fe^{II}(HS)-Fe^{IV}(HS) or Fe^{III}(HS)-Fe^{III}(IS), but not Fe^{III}(HS)-Fe-^{III}(HS). The same conclusions can be deduced intuitively using the localized BS approach (Figures S20-21). With two coupled HS d^5-centres, single electron d-d excitation can have only either of two outcomes (Scheme 3. Excitation with $\Delta m_S = 0$ (BS states are not the Eigenfunctions of S^2), e.g., Scheme 3-a, can be spin-allowed (S=0, $m_S = 0$ ← S=0, $m_S = 0$) or spin forbidden (S=1, $m_S = 0$ ← S=0, $m_S = 0$), and in both cases involve charge transfer. A spin-forbidden excitation ΔM_S=|1|, e.g., Scheme 3-b, leads to a non-symmetrical Fe^{III}(HS)-O-Fe^{III}(IS) system.

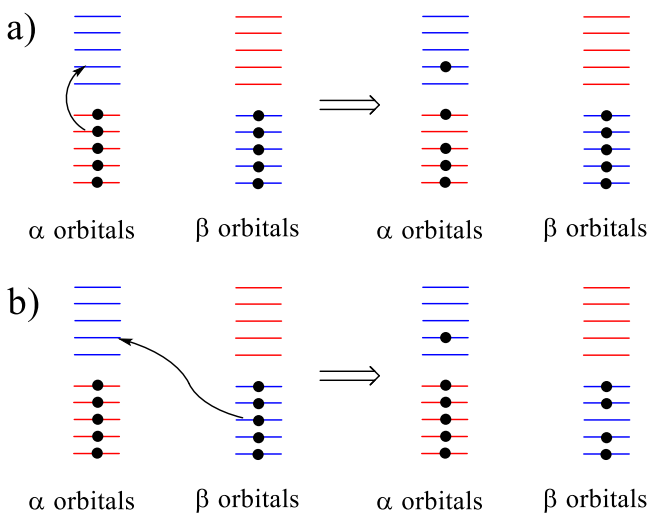

Scheme 3. Possible one electron d-d excitations on [(L)Fe^{III}-μ-O-Fe^{III}(L)]$^{2+}$ (**2a**), in the framework of localized BS orbitals: example of the excitation with $\Delta M_S=0$ (α-α or β-β) and b) example of the excitation $\Delta M_S=|1|$ (α-β or β-α)

In excited states one of the Fe-O bond was elongated, due to loss of the equivalence of the formerly coupled Fe^{III} centres. In the "spin-allowed" charge transfer excitations, charge density changed in the expected manner (assessed by Mulliken and MDC population analysis). The charge spin density was consistent with the (S=2, S=2) charge transfer state obtained and overall these data indicate that "spin-allowed" charge transfer excitation has a clearly dissociative character.

Geometry was optimized with 12 DFAs (BP86, OPBE, PBE, PW91, S12g, B3LYP, PBE0, S12h, M06-L, TPPS, M06 and M06-2X). In the absence of a crystal structure for the dinuclear complex **2a** the geometries obtained where compared with [(N4Py)Fe^{III}(μ-O)Fe^{III}(N4Py))](ClO$_4$)$_2$.[2] that differ only by the absence of methyl group. The results are summarized in Table S3, and indicated that S12g yielded the best structural parameters with smallest MAE and LE. Given the track record of S12g in calculation of spin state energetics,[38] all further electronic structure calculations were performed with this level of theory.

Table S 3 Comparison of bond lengths (Å) in the optimized structures with those of the X-ray crystal structure of $[(N4Py)Fe^{III}(\mu O)Fe^{III}(N4Py))](ClO_4)_2$. Mean absolute error (MAE) and largest absolute error (LAE) are also provided.

Level of theory			Fe_1-O_2	Fe_1-N_3	Fe-$_1N_4$	Fe_1-N_5	MAE	LAE
Singlet $\left(\frac{5}{2},\frac{5}{2};\mathrm{BS}\right)$	GGA	bp86	1.835	2.193	2.209	2.331	0.067	0.087
		opbe	1.835	2.206	2.209	2.304	0.064	0.099
		pbe	1.834	2.191	2.207	2.331	0.066	0.087
		pw91	1.832	2.189	2.202	2.330	0.064	0.086
		S12g	1.803	2.159	2.173	2.296	0.033	0.052
	hybrid	b3lyp	1.846	2.195	2.209	2.320	0.068	0.088
		pbe0	1.828	2.166	2.179	2.289	0.041	0.059
		s12h	1.821	2.165	2.185	2.290	0.041	0.058
	metagga	M06-l	1.834	2.171	2.181	2.317	0.051	0.073
		TPSS	1.837	2.188	2.199	2.306	0.058	0.081
	MetaHYBRID	M06	1.829	2.153	2.172	2.306	0.040	0.062
		M06-2X	1.847	2.156	2.201	2.292	0.049	0.057
Triplet (SA=½, SB=½)	GGA	S12g	1.827	1.991	1.990	2.010	0.132	0.234
Experimental structure			1.803	2.107	2.144	2.244	-	-

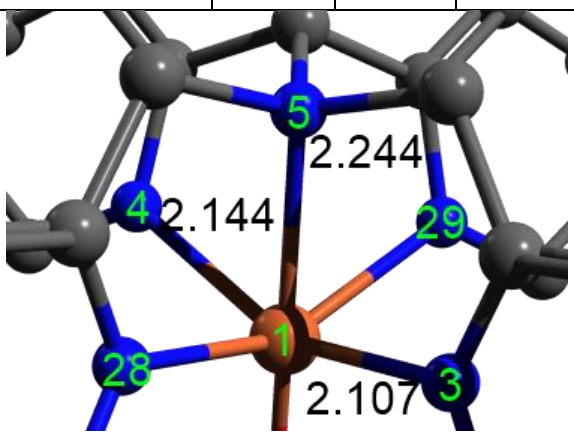

Sequence numbers of first coordination sphere, and bond lengths from the crystal structure, in order to facilitate the analysis of Table S3, the C_{2h} symmetry of **2a** requires only the upper part to be shown. In addition, bonds that are symmetrically identical (Fe_1-N_3 and Fe_1-N_{28}; Fe_1-N_4 and Fe_1-N_{29}).

Spin states of 2a

Table S 4 Relative spin-state energies (kcal/mol) for **2a** Calculations were performed with the S12g/TZ2P level of theory.

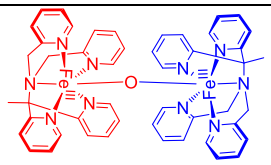								
Spin state {2S+1}[31,32]	Undectet {11}	Nonet {9}	Septet {7}	Quintet {5}	Triplet {3}	Singlet[1] $\left(\frac{5}{2},\frac{5}{2};\mathrm{BS}\right)$ {1}	Singlet[2] $\left(\frac{5}{2},\frac{5}{2};\mathrm{BS}\right)$ {1}	Singlet† $\left(\frac{1}{2},\frac{1}{2};\mathrm{BS}\right)$ {1}
Relative energy	11.30	14.66	5.83	3.45	4.32	4.62	0.00	10.81

All the initial test calculations indicated that the spin state of **2a** is a singlet obtained by antiferromagnetic coupling of two Fe(III) high spin states. Since S12g shows excellent performance for spin state energetics and it provides the optimized geometries that were the closest to the available crystallographic data, the detailed analysis of the close lying spin state was performed with this level of theory. The results are given in Table S4. Since there is a discussion in the literature as to the energy of the BS that should be used as a singlet state or should projective methods be applied,[39–42] both results are given. Inspection of the table indicates that the only state that is close in energy to ($^5/_2$,$^5/_2$;BS) state is a triplet state originating from two ferromagnetically coupled low spin Fe(III) centers. To further test the two close lying candidates for the ground spin state, we compared the triplet state geometry with experimentally obtained structure, Table S3. The agreement was poor, with large deviations in bond lengths.

Dissociated products' spin states

In order to examine the electronic structure of all possible dissociation products (LFe(III)O + LFe(III) and LFe(IV)O + LFe(II)) with and without explicit coordination of CH_3CN solvent molecules, we calculated all available spin states for each structure separately. The results are given in the Tables S5-S10. LFe(IV)O is in the triplet and LFe(III)O is in the quartet ground state, while LFe(III) and LFe(II), with and without the coordinated of CH_3CN are in low spin ground state.

Table S 5 Relative spin-state energies (kcal/mol) for iron(III)-oxo monomeric unit; Calculations were performed with the S12g/TZ2P level of theory.

[1] Spin-projected with Yamaguchi formalism
[2] Non projected

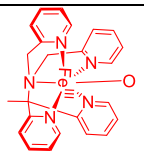

Spin state {2S+1}	Sextet {6}	Quartet {4}	Doublet {2}
Relative energy	-7.98	-10.99	0

Table S 6 Relative spin-state energies (kcal/mol) for pentacoordinated iron(III) monomeric unit; Calculations were performed with the S12g/TZ2P level of theory.

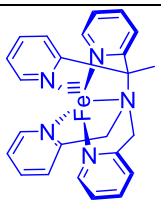

Spin state {2S+1}	Sextet {6}	Quartet {4}	Doublet {2}
Relative energy	9.06	1.34	0

Table S 7 Relative spin-state energies (kcal/mol) for **4**; Calculations were performed with the S12g/TZ2P level of theory.

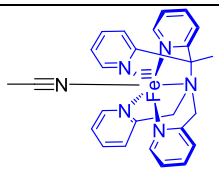

Spin state {2S+1}	Sextet {6}	Quartet {4}	Doublet {2}
Relative energy	15.93	23.88	0

Table S 8 Relative spin-state energies (kcal/mol) for a iron(IV)-oxo monomeric unit; Calculations were performed with the S12g/TZ2P level of theory

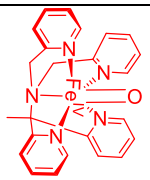

Spin state {2S+1}	Quintet {5}	Triplet {3}
Relative energy	13.48	0

Table S 9 Relative spin-state energies (kcal/mol) for a pentacoordinated iron(II) monomeric unit; Calculations were performed with the S12g/TZ2P level of theory.

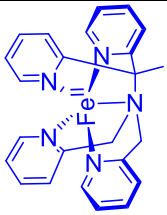

Spin state {2S+1}	Quintet {5}	Triplet {3}	Singlet {1}
Relative energy	7.58	5.15	0

Table S 10 Relative spin-state energies (kcal/mol) a for iron(II) monomeric unit with coordinated CH_3CN; Calculations were performed with the S12g/TZ2P level of theory.

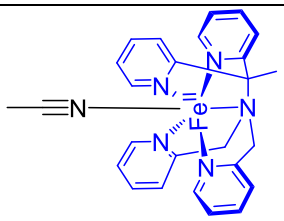

Spin state {2S+1}	Quintet {5}	Triplet {3}	Singlet {1}
Relative energy	18.97	27.29	0

Dissociation thermodynamics

After calculation of the spin ground state of dissociation products, we examined the thermodynamics of dimer dissociation. The electronic energies and Gibbs free energies for the pathways with and without coordination of CH_3CN are given in Tables S11-S14. Inspection of the results demonstrates that both dissociation are stabilized by a solvent coordination by ~30 kcal/mol and that LFe(IV)O + LFe(II) charge transfer path is substantially more favorable. It is also important to notice that, when coordination of CH_3CN is explicitly included, both dimer and monomers are very close in energy.

Table S 11 Energy difference (kcal/mol) between the products and the reactant for the dimer **2a** dissociation reaction to two iron(III) monomeric units.

Heterolytic bond cleavage	Reactant	Product	Product	Total
	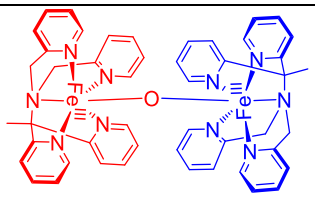	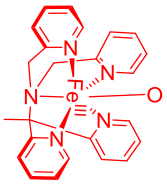	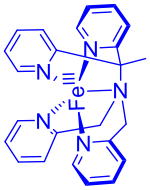	-
Ground spin state	Singlet, $\left(\frac{5}{2},\frac{5}{2};\mathrm{BS}\right)$	Quartet	Doublet	
Electronic energy	-16143.66	-8228.53	-7848.59	66.54
Gibbs free energy	-15656.05	-7993.09	-7613.01	49.95

Table S 12 Energy difference (kcal/mol) between the products and the reactants for the dimer **2a** dissociation reaction to two iron(III) monomeric units, with explicit coordination of $CN_3C{\equiv}N$ solvent molecule.

Heterolytic bond cleavage	Reactant	Reactant	Product	Product	Total
	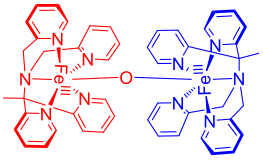		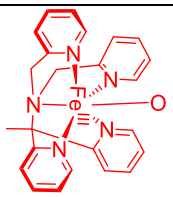	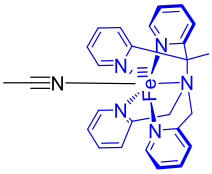	-
Ground spin state	Singlet, $\left(\frac{5}{2},\frac{5}{2};\mathrm{BS}\right)$	Singlet	Quartet	Doublet	
Electronic energy	-16143.66	-860.81	-8228.53	-8740.98	34.96
Gibbs free energy	-15656.05	-847.50	-7993.09	-8477.14	33.32

Table S 13 Energy difference (kcal/mol) between the products and the reactant for the dimer **2a** dissociation reaction to two iron(IV) and iron(II) monomeric units, with explicit coordination of CN3C≡N.

Homolytic bond cleavage	Reactant	Product	Product	Total
	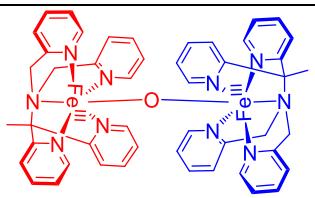	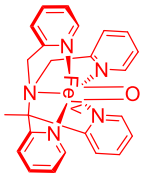	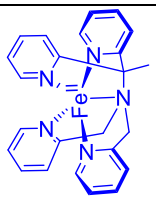	
Ground spin state	Singlet, $\left(\frac{5}{2},\frac{5}{2};\mathrm{BS}\right)$	Triplet	Singlet	
Electronic energy	-16143.66	-8130.56	-7974.38	38.72
Gibbs free energy	-15656.05	-7892.78	-7738.21	25.06

Table S 14 Energy difference (kcal/mol) between the products and the reactant for dissociation of 2a to two iron(IV) and iron(II) monomeric units.

Homolytic bond cleavage	Reactant	Reactant	Product	Product	Total
	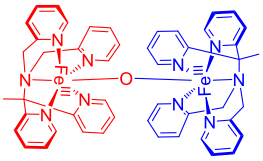		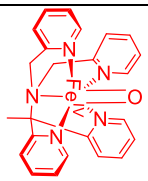	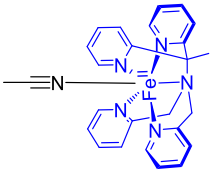	
Ground spin state	Singlet, $\left(\frac{5}{2},\frac{5}{2};\mathrm{BS}\right)$	Singlet	Triplet	Singlet	
Electronic energy	-16143.66	-860.81	-8130.56	-8867.67	6.24
Gibbs free energy	-15656.05	-847.50	-7892.78	-8605.78	4.99

Broken Symmetry solution

The magnetic behavior of coupled, spatially separated, local spins is commonly modeled using phenomenological Heisenberg-Dirac Hamiltonian,[43] that reduces complicated quantum mechanical problem to a simplified description in terms of spin degrees of freedom only. For a system that consist of two metal (or radical) centers it can be written as:

$$\hat{H} = -J\,\hat{S}_A \cdot \hat{S}_B \qquad (1)$$

where $\hat{S}_A$ and $\hat{S}_B$ are spin-operators associated with the spin-moments of unpaired electrons residing on spin-centers A and B. Only the total spin is physical observable, and in the case of two local spins, the possible total spins are given by Clebsch-Gordan Series: S_A+S_B, S_A+S_B-1, …, $|S_A+S_B|$. The two spin-centers are described as ferromagnetically aligned when they produce the maximum total spin ($S_A^{\uparrow},S_B^{\uparrow}$), and antiferromagnetically aligned when they produce minimum total spin ($S_A^{\uparrow},S_B^{\downarrow}$). The J is the magnetic coupling parameter, which measures the strength of isotropic XC interaction (is positive for ferromagnetic and negative for antiferromagnetic alignment). Thus, by knowing J, it is possible to qualitatively account for the observed magnetic properties of the system. Currently the standard method for determining J is by mapping differences in calculated total energies from electronic structure calculations onto the spin-states from eq. 1.[44]

The problem arises from the fact that only the ferromagnetically coupled ($S_{MAX}=S_A+S_B$) state can be properly described by one Slater determinant. This instantly leads to the conclusion that multideterminental methodologies that are based on configuration interaction,[45,46] should be used. Unfortunately, such methodologies are usually too computationally demanding to study the large di- and poly nuclear TM complexes, or even the relatively small systems with many unpaired electrons (such as „small" Fe(III)–Fe(III) dimers) are currently unfeasable.[43] Another drawback is the fact that these systems often possess considerable dynamical correlation, which makes the accurate calculations even more difficult.

Although the DFT offers appreciable accuracy at manageable computational scaling, it cannot rigorously describe multideterminantal states. Noodleman's suggestion[47,48] was the approach called the broken-symmetry (BS), that represent multideterminental states with only one „antiferromagnetically coupled" slated determinant. For example, correct spin function for two unpaired electrons on sites A and B can be constructed using Clebsch-Gordan coefficients, and is given below:

$$\psi(S_A=1, S_B=1, S=0) = (1/2\sqrt{3})\left(2\left|A^{\uparrow\uparrow}B^{\downarrow\downarrow}\right| + 2\left|A^{\downarrow\downarrow}B^{\uparrow\uparrow}\right| - \left|A^{\uparrow\downarrow}B^{\uparrow\downarrow}\right| - \left|A^{\uparrow\downarrow}B^{\downarrow\uparrow}\right| - \left|A^{\downarrow\uparrow}B^{\uparrow\downarrow}\right| - \left|A^{\downarrow\uparrow}B^{\downarrow\uparrow}\right|\right) \qquad (2)$$

BS description of this multideterminental state would be simply $\left|A^{\uparrow\uparrow}B^{\downarrow\downarrow}\right|$, but this single determinant is only eigenfuncion of total $\hat{S}_Z$ and not $\hat{S}^2$ (this approach breaks the spin symmetry, hence the name broken-symmetry). One of the artifacts that comes as a consequence of this is the appearance spin density on sites A and B, although the real singlet state should have spin density equal to zero in any point.[49,50] The key step of the methodology is that orbitals are allowed to relax from the starting form under the action of the variational principle.[43,51] Thus, system is given the additional variational flexibility to lower its energy, and the ground state is formed variationaly as a mixture of ferromagnetic state and singlet stats generated by charge-transfer (ionic states).[43,51] Although this process is essentially similar to CI, the BS formalism does not have enough flexibility and it can only mix single determinant ferromagnetic and ionic states,

and the real ground state, multideterminental singlet, is not included in a final result. Qualitatively, BS method yields a correct charge density, but, as previously mentioned, there is a fictitious spin density[3].[49,50]

Justification for utilization for broken symmetry excitations

The same conclusions, regarding the nature of single excitation transitions, can be more intuitively deduced if we start from the localized BS picture. Of course, we first need to explain why we are even qualitatively trying to extract conclusions from obviously erroneous and unphysical starting point! When we consider the possible couplings of two d^5 centers, there are many available options:

$$Fe(\mathrm{III})_{HS}, Fe(\mathrm{III})_{HS} \Rightarrow (5/2, 5/2), \quad Fe(\mathrm{III})_{HS}, Fe(\mathrm{III})_{IS} \Rightarrow (5/2, 3/2), \quad Fe(\mathrm{III})_{IS}, Fe(\mathrm{III})_{IS} \Rightarrow (3/2, 3/2), \ldots$$
$$\ldots, \quad Fe(\mathrm{IV})_{HS}, Fe(\mathrm{II})_{HS} \Rightarrow (2, 2), \quad Fe(\mathrm{IV})_{HS}, Fe(\mathrm{II})_{IS} \Rightarrow (2, 1), \ldots$$

Only the state with maximum spin multiplicity ($S_{MAX}=S_A+S_B$) can be properly represented by one Slater determinant, and for all the other states we are forced to use BS(or some similar) methodology. They are essentially obtained by variation in the population of localized two center d-orbitals manifold (shown on Figure S 28), schematically represented in the left part of the Fig Figure S 29.

The MO diagram (Figure S28) clearly shows that three (out of five) MOs include a significant oxygen contribution. The interaction between the metal centres can be described as π-antibonding (two) and σ-antibonding (one) and hence excitation from nonbonding to antibonding orbitals are expected to lead to Fe^{III}-O bond dissociation.

[3] that is not entirely unphysical since it indicates the distribution of 'effectively unpaired' electrons

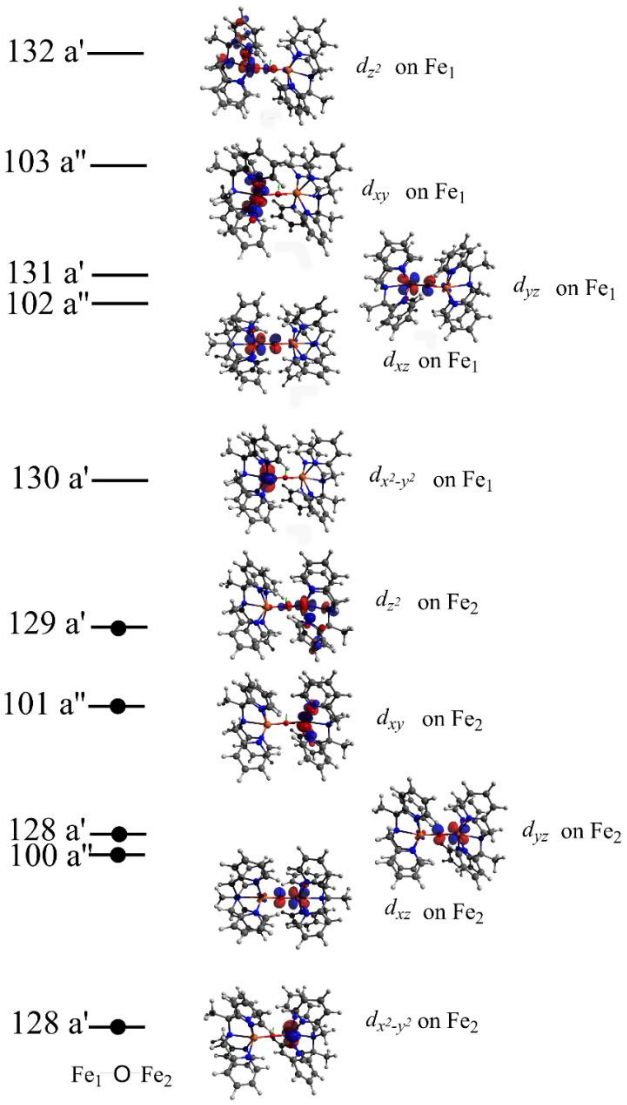

Figure S 27. BS localized molecular orbitals in β-spin for dimer **2a** with S12g/TZ2P level of theory. Orbitals in α-spin are analogous but localized on other centre. The energy separation is not proportional. The nature of the dominant *d* orbitals is depicted.

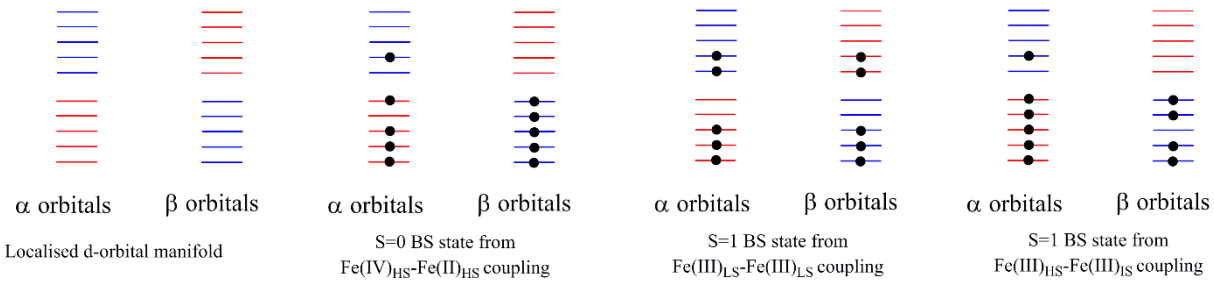

Figure S 28. Schematic representation of some BS solutions that are one of the options to describe multideterminental spin states originating from two centre coupling.

All the BS Slater determinants can be interconverted by simple one or multi electron excitations in the same localized d orbital framework (followed by a variational orbital relaxation). In other words, the approximations we use in order to describe multideterminental spin states originating from coupling of two distant spin centers can be obtained by simple electron excitations in the same localized manifold.

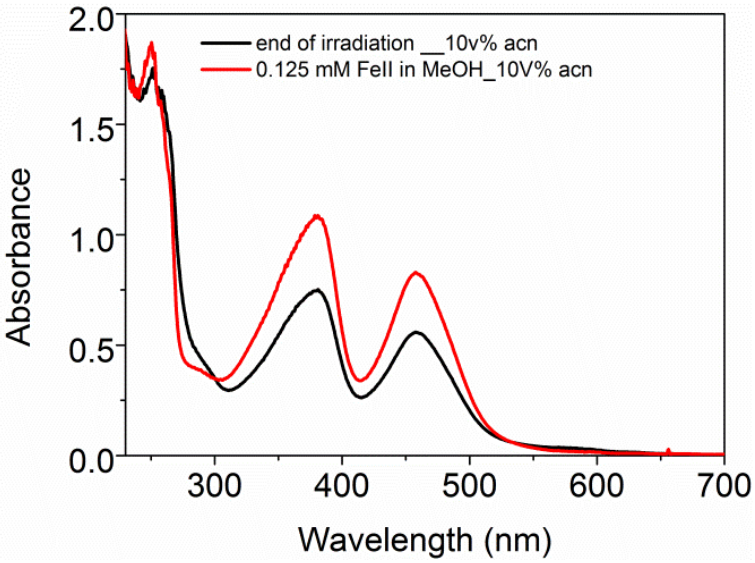

Figure S 29. UV-vis absorption spectrum of **1** (0.125 mM) in methanol after 3 h irradiation under aerobic conditions and after addition of 10 vol% acetonitrile (red).

References

[1] A. Draksharapu, Q. Li, H. Logtenberg, T. A. van den Berg, A. Meetsma, J. S. Killeen, B. L. Feringa, R. Hage, G. Roelfes, W. R. Browne, *Inorg. Chem.* **2012**, *51*, 900–913.
[2] G. Roelfes, M. Lubben, K. Chen, R. Y. N. Ho, A. Meetsma, S. Genseberger, R. M. Hermant, R. Hage, S. K. Mandai, V. G. Young Jr., Y. Zang, H. Kooijman, A. L. Spek, L. Que, Jr., B. L. Feringa., *Inorg. Chem.* **1999**, *38*, 1929–1936.
[3] A. Draksharapu, D. Angelone, M. G. Quesne, S. K. Padamati, L. Gómez, R. Hage, M. Costas, W. R. Browne, S. P. de Visser, *Angew. Chemie Int. Ed.* **2015**, *54*, 4357–4361.
[4] U. Bruker, (2016). APEX3 (v2012.4-3), SAINT (Version 8.18C) and SADABS (Version 2012/1). Bruker AXS Inc., Madison, Wisconsin, **n.d.**
[5] F. G. Kari, S. Hilger, S. Canonica, *Environ. Sci. Technol.* **1995**, *29*, 1008–1017.
[6] S. Malkin, E. Fischer, *J. Phys. Chem.* **1962**, *66*, 2482–2486.
[7] T. Nash, *Biochem. J.* **1953**, *55*, 416–421.
[8] E. J. Baerends, J. Autschbach, A. Berces, C. Bo, P. M. Boerrigter, L. Cavallo, D. P. Chong, L. Deng, R. M. Dickson, D. E. Ellis, et al., **20016**.
[9] G. te Velde, F. M. Bickelhaupt, E. J. Baerends, C. Fonseca Guerra, S. J. A. van Gisbergen, J. G. Snijders, T. Ziegler, *J. Comput. Chem.* **2001**, *22*, 931–967.
[10] E. Van Lenthe, E. J. Baerends, *J. Comput. Chem.* **2003**, *24*, 1142–1156.
[11] J. P. Perdew, *Phys. Rev. B* **1986**, *33*, 8822–8824.
[12] A. D. Becke, *Phys. Rev. A* **1988**, *38*, 3098–3100.
[13] M. Swart, A. W. Ehlers, K. Lammertsma, *Mol. Phys.* **2004**, *102*, 2467–2474.
[14] Y. Zhang, A. Wu, X. Xu, Y. Yan, *Chem. Phys. Lett.* **2006**, *421*, 383–388.
[15] J. P. Perdew, K. Burke, Y. Wang, *Phys. Rev. B* **1996**, *54*, 16533–16539.
[16] J. P. Perdew, K. Burke, M. Ernzerhof, *Phys. Rev. Lett.* **1997**, *78*, 1396.
[17] J. P. Perdew, *Electronic Structure of Solids' 91*, Akademie Verlag, Berlin, **1991**.
[18] J. P. Perdew, J. A. Chevary, S. H. Vosko, K. A. Jackson, M. R. Pederson, D. J. Singh, C. Fiolhais, *Phys. Rev. B* **1992**, *46*, 6671–6687.
[19] J. P. Perdew, J. A. Chevary, S. H. Vosko, K. A. Jackson, M. R. Pederson, D. J. Singh, C. Fiolhais, *Phys. Rev. B* **1993**, *48*, 4978.
[20] M. Swart, *Chem. Phys. Lett.* **2013**, *580*, 166–171.
[21] A. D. Becke, *J. Chem. Phys.* **1993**, *98*, 5648–5652.
[22] C. Adamo, V. Barone, *J. Chem. Phys.* **1999**, *110*, 6158–6170.
[23] yan zhao, D. G. Truhlar, *J. Chem. Phys.* **2006**, *125*, 194101.
[24] Y. Zhao, D. G. Truhlar, *Theor. Chem. Acc.* **2008**, *120*, 215–241.
[25] J. M. Tao, J. P. Perdew, V. N. Staroverov, G. E. Scuseria, *Phys. Rev. Lett.* **2003**, *91*, 146401.
[26] A. D. Becke, *J. Chem. Phys.* **1988**, *88*, 2547–2553.
[27] M. Franchini, P. H. T. Philipsen, L. Visscher, *J. Comput. Chem.* **2013**, *34*, 1819–1827.
[28] A. Klamt, G. Schuurmann, *J. Chem. Soc. Perkin Trans. 2* **1993**, 799–805.
[29] A. Klamt, *J. Phys. Chem.* **1995**, *99*, 2224–2235.
[30] A. Klamt, V. Jonas, *J. Chem. Phys.* **1996**, *105*, 9972–9981.
[31] C. C. Pye, T. Ziegler, *Theor. Chem. Acc.* **1999**, *101*, 396–408.
[32] M. Swart, E. Rösler, F. M. Bickelhaupt, *Eur. J. Inorg. Chem.* **2007**, *2007*, 3646–3654.
[33] E. van Lenthe, E. J. Baerends, J. G. Snijders, *J. Chem. Phys.* **1993**, *99*, 4597–4610.
[34] E. van Lenthe, E. J. Baerends, J. G. Snijders, *J. Chem. Phys.* **1994**, *101*, 9783–9792.
[35] E. van Lenthe, A. Ehlers, E.-J. Baerends, *J. Chem. Phys.* **1999**, *110*, 8943–8953.
[36] D.-J. Chen, Y. Y. J. Tong, *Chem. Commun.* **2015**, *51*, 5683–5686.
[37] V. Balland, F. Banse, E. Anxolabéhère-Mallart, *Inorg. Chem.* **2003**, *42*, 2470–2477.
[38] M. Gruden, S. Stepanovic, M. Swart, *J. Serbian Chem. Soc.* **2015**, *80*, 1399–1410.
[39] R. Caballol, O. Castell, F. Illas, I. de P. R. Moreira, J. P. Malrieu, *J. Phys. Chem. A* **1997**, *101*, 7860–7866.
[40] C. Adamo, V. Barone, A. Bencini, R. Broer, M. Filatov, N. M. Harrison, F. Illas, J. P. Malrieu, I. de P. R. Moreira, *J. Chem. Phys.* **2006**, *124*, 107101.
[41] E. Ruiz, J. Cano, S. Alvarez, V. Polo, *J. Chem. Phys.* **2006**, *124*, 107102.
[42] E. Ruiz, *J. Comput. Chem.* **2011**, *32*, 1998–2004.
[43] F. Neese, *Coord. Chem. Rev.* **2009**, *253*, 526–563.
[44] J. J. Phillips, J. E. Peralta, *J. Phys. Chem. A* **2014**, *118*, 5841–5847.
[45] V. M. García, O. Castell, R. Caballol, J. P. Malrieu, *Chem. Phys. Lett.* **1995**, *238*, 222–229.
[46] T. Helgaker, P. Jorgensen, J. Olsen, *Molecular Electronic-Structure Theory*, Wiley, **2008**.
[47] L. Noodleman, *J. Chem. Phys.* **1981**, *74*, 5737–5743.
[48] L. Noodleman, E. J. Baerends, *J. Am. Chem. Soc.* **1984**, *106*, 2316–2327.
[49] V. N. Staroverov, E. R. Davidson, *Chem. Phys. Lett.* **2000**, *330*, 161–168.
[50] M. Head-Gordon, *Chem. Phys. Lett.* **2003**, *372*, 508–511.
[51] F. Neese, *J. Phys. Chem. Solids* **2004**, *65*, 781–785.